

# Synergistic Enhancement of Intragrain Kinetics and Interfacial Stability in Cr-Doped VO<sub>2</sub>@Carbon Cathode Enabling Advanced Aqueous Zinc-Metal Batteries

Peixi Li, Huihan Yang, Wenwei Zhang, Shijie Dong, Ping Luo,\* and Qinyou An\*

VO<sub>2</sub> has gained attention as a promising cathode material owing to its favorable ion diffusion pathways and abundant valence states. However, its performance is hindered by sluggish kinetics from zinc ions, high charge density, and vanadium dissolution induced by reactive water. Herein, Cr, ion doping is utilized to modulate the local electronic structure, enhancing zinc-ion diffusion. Additionally, a carbon-coating strategy is applied to reduce

vanadium dissolution from excessive water-VO<sub>2</sub> contact. This dual-modification approach enables VO<sub>2</sub> to achieve exceptional rate capability and capacity retention, demonstrating 70% capacity retention after 1000 cycles at 3 A g<sup>-1</sup>. Moreover, Zn<sup>2+</sup> diffusion in VO<sub>2</sub> after the Cr-doping and carbon-coating is significantly improved compared to pure VO<sub>2</sub>. These findings offer new insights into optimizing metal-ion battery cathode materials.

## 1. Introduction

In recent years, VO<sub>2</sub> has been extensively investigated as a cathode material for aqueous zinc-metal batteries, attributed to its appropriate pore structure and the multiple valence states of the vanadium element.<sup>[1]</sup> However, the high charge density of zinc ions often leads to their sluggish diffusion within the VO<sub>2</sub> lattice, thereby impairing the rate capability. Moreover, the high polarity of water molecules continually assaults the VO<sub>2</sub> surface, especially under the influence of an electric field, triggering severe vanadium dissolution that ultimately causes material degradation.<sup>[2]</sup> Consequently, adopting appropriate modification strategies to mitigate these intractable problems will significantly enhance the zinc storage capability of VO<sub>2</sub>.

On one hand, in addressing the issue of vanadium dissolution in VO<sub>2</sub>, electrolyte strategies can suppress vanadium dissolution by reducing water activity and water content at the solid–liquid interface.<sup>[3]</sup> However, such strategies have little to no positive impact on zinc-ion transport within the VO<sub>2</sub> lattice. On the other hand, for improving the electrical/ion conductivity of VO<sub>2</sub>, three

mainstream strategies are conductive material compositing,<sup>[4]</sup> oxygen vacancy modulation,<sup>[5]</sup> and heteroatom doping.<sup>[6]</sup> Typically, compositing VO<sub>2</sub> with materials such as graphene can construct an efficient electron-transport network, reducing polarization.<sup>[7]</sup> However, such composites often exhibit uneven coating, and weak interfacial interactions may lead to unstable performance. Moreover, this strategy has a minimal impact on the intrinsic conductivity of the internal crystal structure. Second, oxygen vacancies can act as electron traps to facilitate electron transport and serve as active sites.<sup>[8]</sup> However, this atomic-deficiency strategy carries the risk of potential structural instability. During prolonged cycling, oxygen vacancies may be oxidized, leading to performance degradation. Additionally, heteroatom doping can modulate the electronic structure, enhancing its intrinsic conductivity, promoting electron transport, and suppressing structural collapse during charge/discharge processes, thereby improving cyclic stability.<sup>[9]</sup> However, trace doping levels are insufficient to protect the VO<sub>2</sub>–electrolyte interface, and interstitial doping risks atom desorption or strong electrostatic interactions with zinc ions.

Drawing from the above discussion and existing literature, it is evident that single-strategy modifications often fall short of harnessing synergistic effects. Therefore, a dual-pronged approach, simultaneously optimizing the electrode material's internal structure and the electrode–electrolyte interface is critical to enhancing the zinc storage capability of the promising VO<sub>2</sub> cathode for aqueous zinc-metal battery.<sup>[10]</sup> However, this comprehensive strategy remains underexplored.

Among common transition metal ions (such as Cr<sup>3+</sup>, Mn<sup>2+</sup>, and Co<sup>3+</sup> ions explored for doping vanadium oxide cathode materials), chromium ions present distinctive advantages of ionic radius and electron structure. Herein, as shown in Figure 1, Cr<sup>3+</sup> (ionic radius of 0.64 Å), which has a similar ionic radius to V<sup>4+</sup> (0.54 Å), is selected to substitute V-atom sites, minimizing lattice distortion and preserving the structural integrity of VO<sub>2</sub>, which can reduce structural collapse caused by volume expansion during

P. Li, S. Dong, P. Luo

School of Materials and Chemical Engineering

Hubei University of Technology

Wuhan 430068, China

E-mail: blueknight\_0930@163.com

H. Yang, S. Dong

School of Mechanical Engineering

Wuhan Polytechnic University

Wuhan 430023, P. R. China

W. Zhang, Q. An

State Key Laboratory of Advanced Technology for Materials Synthesis and Processing

Wuhan University of Technology

Wuhan 430070, P. R. China

E-mail: anqinyou86@whut.edu.cn



Supporting information for this article is available on the WWW under <https://doi.org/10.1002/batt.202500333>

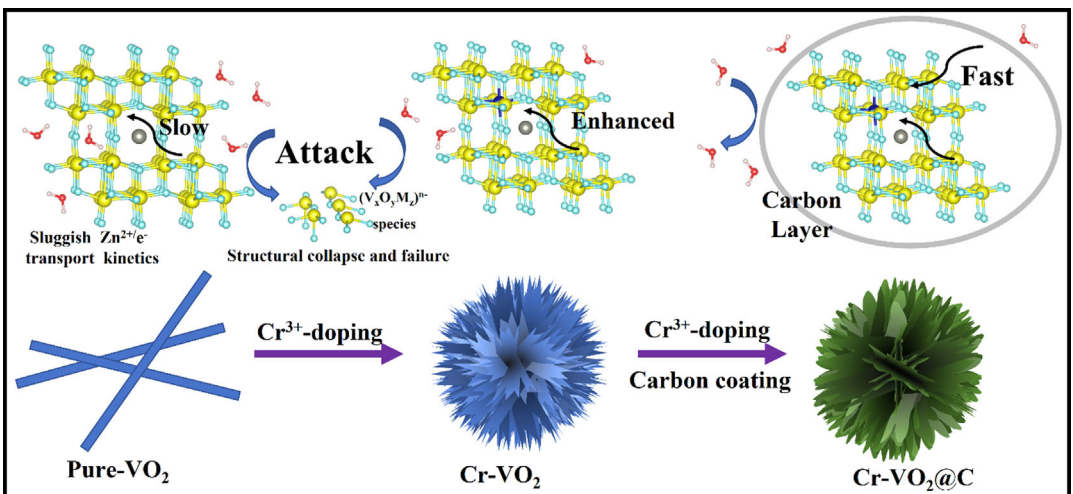


**Figure 1.** Schematic diagram of the challenges and modification mechanisms in  $\text{VO}_2/\text{Zinc}$  battery.

charge/discharge cycles. Furthermore, an *in situ* carbon-coating strategy is employed to isolate active water from direct contact with  $\text{VO}_2$  while further enhancing electrical conductivity.  $\text{VO}_2$  modified with this dual protection strategy—targeting both intra-crystalline and solid–liquid interfaces—exhibits superior cyclic stability and rapid zinc-ion diffusion kinetics.

## 2. Results and Discussion

### 2.1. Characterization of Cathode Materials

Based on the above discussion, the pure, Cr-doped, as well as Cr-doping and carbon-coating modified  $\text{VO}_2$  were synthesized through a simple hydrothermal method. The crystal structure of as-prepared  $\text{VO}_2$ ,  $\text{CrVO}_2$  ( $\text{CrVO}$ ), and  $\text{CrVO}_2@\text{C}$  ( $\text{CrVO}@C$ ) cathode materials was verified by using of X-ray diffraction (XRD) (Figure 2a), with all diffraction peaks matching the monoclinic structure of the  $\text{VO}_2$  standard card (PDF#82-2392). In this case, the decreased intensity of all crystal planes is attributed to the disorder state induced after doping of  $\text{Cr}^{3+}$  and carbon coating.<sup>[11]</sup> Moreover, the introduction of  $\text{Cr}^{3+}$  can transform the nanobelts of  $\text{VO}_2$  into a nanoflower morphology due to the change in surface formation energy. Furthermore, after the subsequent introduction of a carbon source, the fluffy nanoflower spheres are transformed into nanoflowers with rough surfaces, which can be attributed to factors such as the change in solution viscosity (Figure 2b–d).<sup>[12]</sup> This nanoflower structure could increase the contact area between the electrode and electrolyte, which enhances the ion diffusion process.<sup>[13]</sup> Meanwhile, the specific chemical formula of  $\text{CrVO}@C$  was determined by ICP test (Table S1, Supporting Information) as  $\text{Cr}_{0.056}\text{V}_{0.95}\text{O}_2\cdot\text{nH}_2\text{O}@C$ .

The Raman spectrum of prepared cathode materials was shown in Figure 2e, compared to the  $\text{VO}_2$  and  $\text{CrVO}$ , the  $\text{CrVO}@C$  exhibited D- and G band bending vibrations at 1350 and 1596  $\text{cm}^{-1}$ , respectively, which can be attributed to the presence of carbon, thereby confirming the successful coating of carbon. Furthermore, the observed changes in Raman shift and

intensity between  $\text{CrVO}$  and  $\text{CrVO}@C$  with pure  $\text{VO}_2$  demonstrate an alteration in the local structure induced by the introduction of  $\text{Cr}^{3+}$  ions. Moreover, Infrared spectroscopy further confirmed the presence of the carbon-coating layer in  $\text{CrVO}@C$ , as shown in Figure S1, Supporting Information. Specifically, a characteristic peak ascribed to the C–O bond was detected at 1709.14  $\text{cm}^{-1}$ . Additionally, the observed shift in this peak aligns with the Raman spectroscopy results, consistently demonstrating the successful incorporation of  $\text{Cr}^{3+}$  ions.

Moreover, the composition and valence state of elements in  $\text{VO}_2$  and  $\text{CrVO}_2@\text{C}$  were investigated using X-ray photoelectron spectroscopy (XPS) analysis, the full spectrum of the  $\text{CrVO}@C$  cathode material in Figure 2f mainly contains Cr, V, O, and C elements. As shown in Figure 2g, the peaks mainly correspond to the V 2p 3/2 and V 2p 1/2 of  $\text{V}^{4+}$ . Following the incorporation of  $\text{Cr}^{3+}$  ions and a carbon layer, the  $\text{V}^{4+}$  binding energy exhibited a slight shift from 514.75 to 515.00 eV. This shift indicates a local electronic reorganization to maintain electroneutrality within the doped  $\text{VO}_2$  material, induced by the reducing effect of the  $\text{Cr}^{3+}$  ions.<sup>[14]</sup> Also, the peaks at 574.8 and 583.6 eV in Figure 2h correspond to  $\text{Cr}^{3+}$  2p 3/2 and  $\text{Cr}^{3+}$  2p 1/2, respectively, which proves the successful introduction of  $\text{Cr}^{3+}$  ion into  $\text{VO}_2$ . Therefore, the above characterization results clearly demonstrate that a carbon-coating layer and Cr ions had been successfully introduced into  $\text{VO}_2$ , exhibiting high uniformity and sample purity.

### 2.2. Electrochemical Performance

The comparisons of cyclic voltammetry (CV) curves for  $\text{VO}_2$ ,  $\text{CrVO}$ , and  $\text{CrVO}@C$  were obtained (Figure 3a). The integral area of the CV curve correlates directly with the reversible capacity of the electrode material, signifying that a larger area corresponds to a higher charge storage capacity per unit mass or volume. Among the three cathode materials studied,  $\text{CrVO}@C$  exhibits the largest CV curve area. This significant enhancement is primarily attributable to the synergistic effect of  $\text{Cr}^{3+}$  ion doping and carbon layer coating to enhance conductivity and suppress

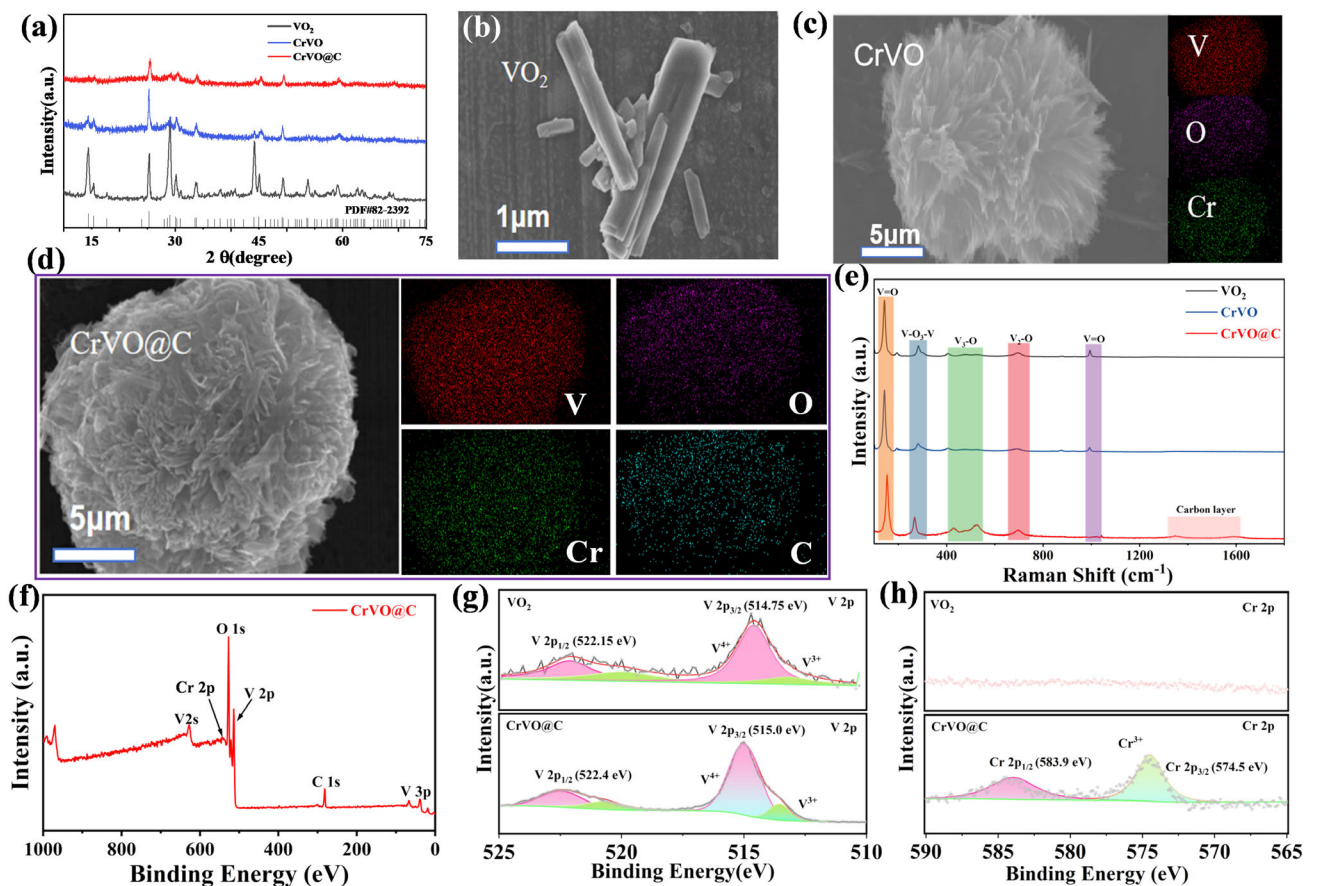


**Figure 2.** a) XRD pattern of proposed cathode materials. b) Scanning electron microscopy (SEM) of pure-VO<sub>2</sub>. c,d) SEM and Mapping of CrVO and CrVO@C. e) Raman spectra of VO<sub>2</sub>, CrVO, and CrVO@C. f) The full CV XPS spectra of CrVO@C. g,h) XPS of V 2p, and Cr 2p of VO<sub>2</sub> and CrVO@C.

vanadium dissolution. Expectantly, these modifications substantially improve the electrochemical performance of the VO<sub>2</sub> cathode. Notably, the CV curve of CrVO@C exhibits good reversibility when compared to that of VO<sub>2</sub> and CrVO, which may predict excellent cycling stability (Figure 3b and S2, Supporting Information).

Further, Figure 3c presents the rate performance of the three cathodes, evaluated at progressively increasing current densities: 0.1, 0.3, 0.5, 0.7, 1.0, and 3.0 A g<sup>-1</sup>. Notably, while the CrVO@C cathode initially displayed a specific capacity similar to the others within the first 10 cycles, it subsequently maintained the highest specific capacity across the tested current densities. As the current density increased, the specific capacity of bare CrVO declined slowly than that of VO<sub>2</sub>, indicating that the doping of Cr<sup>3+</sup> ions significantly enhances the electrical conductivity and structure stability of the host material. Moreover, CrVO@C exhibited superior rate performance compared to CrVO and VO<sub>2</sub>, demonstrating that the synergistic effect of Cr<sup>3+</sup> ion doping and carbon coating substantially improves the performance of VO<sub>2</sub> at high current densities. The CrVO had higher voltage platform than that of VO<sub>2</sub> and CrVO@C in Figure 3d, which could be attributed to the fact that carbon layer may cover some of the active sites of VO<sub>2</sub>, reducing its direct contact with the electrolyte and inhibiting side reactions under high voltage, resulting in a slight decrease in the overall voltage platform. Further, the cycling stability of the battery was tested

during a long cycling process (Figure 3e), showing that CrVO@C retains 70% of its capacity after 1300 cycles.

Additionally, the uncontrollable dissolution of vanadium is the main contributor to the poor cycling stability of vanadium-based cathode materials.<sup>[15]</sup> At low current densities, the direct cause of the rapid capacity decay is the structural collapse. In most scenarios, the dissolution of vanadium ultimately results in the structural disintegration of the material and battery failure, as it induces irreversible breaking and rearrangement of internal bonds.<sup>[16]</sup> This issue is further exacerbated during cycling at low current densities. As shown in Figure 3f, CrVO@C exhibits a considerable specific capacity of 248.1 mAh g<sup>-1</sup> and maintains a high capacity retention of 82.7% after 100 cycles, demonstrating superior capacity and cycling stability compared to VO<sub>2</sub>. It can also be seen from the charge-discharge curves (Figure 3g) that the CrVO@C cathode exhibits slow capacity decays over the first fifty cycles. The above increased specific capacity and cycling stability could be attributed to the enhanced ion diffusion by the introduction of Cr<sup>3+</sup> and the suppressed vanadium dissolution by the Carbon-based screen water layer.

### 2.3. Kinetics of Zinc-Ion Transport Process

Electrochemical impedance spectroscopy was used to characterize the charge transfer resistance (RCT) of VO<sub>2</sub> and CrVO@C

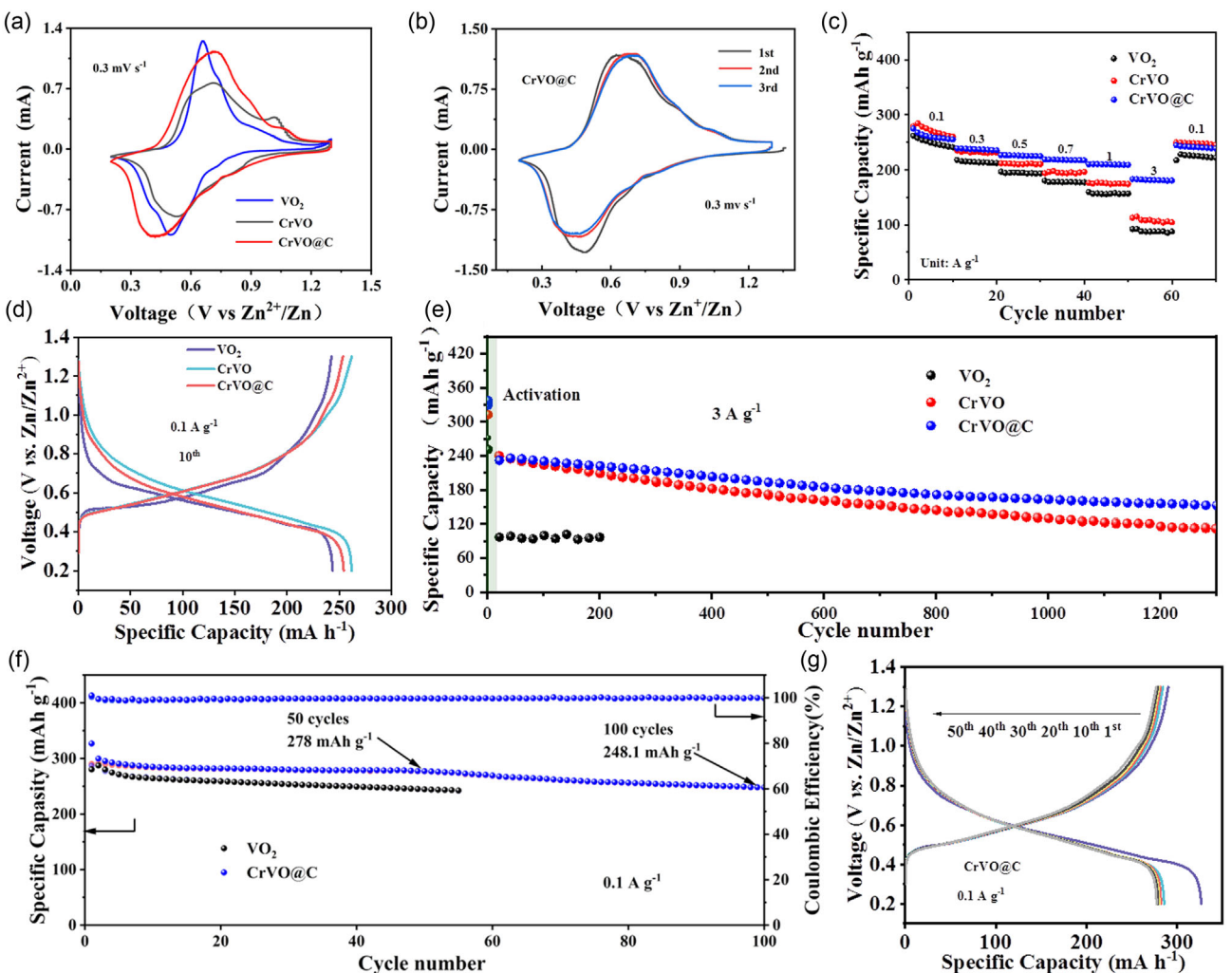


**Figure 3.** a) CV curves of the VO<sub>2</sub>, CrVO, and CrVO@C at 0.3 mV s<sup>-1</sup>. b) CV curve of the CrVO@C during the initial three cycles at 0.3 mV s<sup>-1</sup>. c) Rate performance of the VO<sub>2</sub>, CrVO, and CrVO@C. d) Galvanostatic charge–discharge curves of VO<sub>2</sub>, CrVO, and CrVO@C at 10th cycles. e) Cycling performance of VO<sub>2</sub>, CrVO, and CrVO@C at 3 A g<sup>-1</sup>. f) Cycling performance of VO<sub>2</sub> and CrVO@C at 0.1 A g<sup>-1</sup>. g) Charge–discharge curve of CrVO@C for the initial fifty cycles.

cathodes (Figure 4a). The latter had clearly decreased charge transfer resistance, which could be attributed to the improved electron conductivity by the double strategy and achieved faster mass-transfer process. Furthermore, using the galvanostatic intermittent titration technique (GITT), the diffusion coefficient of Zn<sup>2+</sup> ( $D_{\text{Zn}^{2+}}$ ) in the VO<sub>2</sub> and CrVO@C cathodes was accurately measured.  $D_{\text{Zn}^{2+}}$  can be calculated using the following equation.

$$D_{\text{Zn}^{2+}} = \frac{4}{\pi \tau} \left( \frac{m_B V_B}{M_B S} \right)^2 \left( \frac{\Delta E_s}{\Delta E_t} \right)^2$$

In this formula,  $\tau$  represents the relaxation time (s), while  $S$  represents the contact area between the electrode sheet and the electrolyte (cm<sup>2</sup>).  $m_B$  and  $V_B$  correspond to the number of moles of the electrode material (mol) and the molar volume (cm<sup>3</sup> mol<sup>-1</sup>);  $\Delta E_s$  and  $\Delta E_t$  are the voltage changes (V) caused by the constant current pulse and the voltage change (V) induced by constant current charge–discharge, respectively. As shown in Figure 4b,c, the CrVO@C had a significantly reduced overpotential than that of VO<sub>2</sub> based on the GITT curves for VO<sub>2</sub> and CrVO@C at

a current density of 0.1 A g<sup>-1</sup>, which is caused by the large change in voltage and the slow ion diffusion in the former cathode.<sup>[17]</sup> Correspondingly, the latter produced faster and more stable diffusion coefficients of zinc ions within the cathode material.

Based on the excellent electrochemical performance of CrVO@C, its energy storage capability was investigated. The CV curves (Figure 4d) of the battery were measured at scan rates of 0.2, 0.4, 0.6, 0.8, and 1.0 mV s<sup>-1</sup>. It can be observed that as the scan rate gradually increases, the CV curves maintain a similar shape and redox peaks, with only slight peak shifts, indicating that the CrVO@C cathode exhibits low polarization and high reversibility. Moreover, the calculated  $b$  values for peak  $a$  and peak  $b$  are 0.73 and 0.74 for the CrVO@C cathode, respectively (Figure 4e). This shows that the electrochemical reaction of CrVO@C is controlled by the capacitive and diffusion processes, and the former can further improve the ion diffusion.<sup>[18]</sup> Correspondingly, the capacitance contribution of VO<sub>2</sub> rises from 36% to 82%. In contrast, the capacitance contribution rate of CrVO@C gradually increases from 63% to 90%, significantly higher than that of the VO<sub>2</sub> cathode (Figure 4f). Typically,

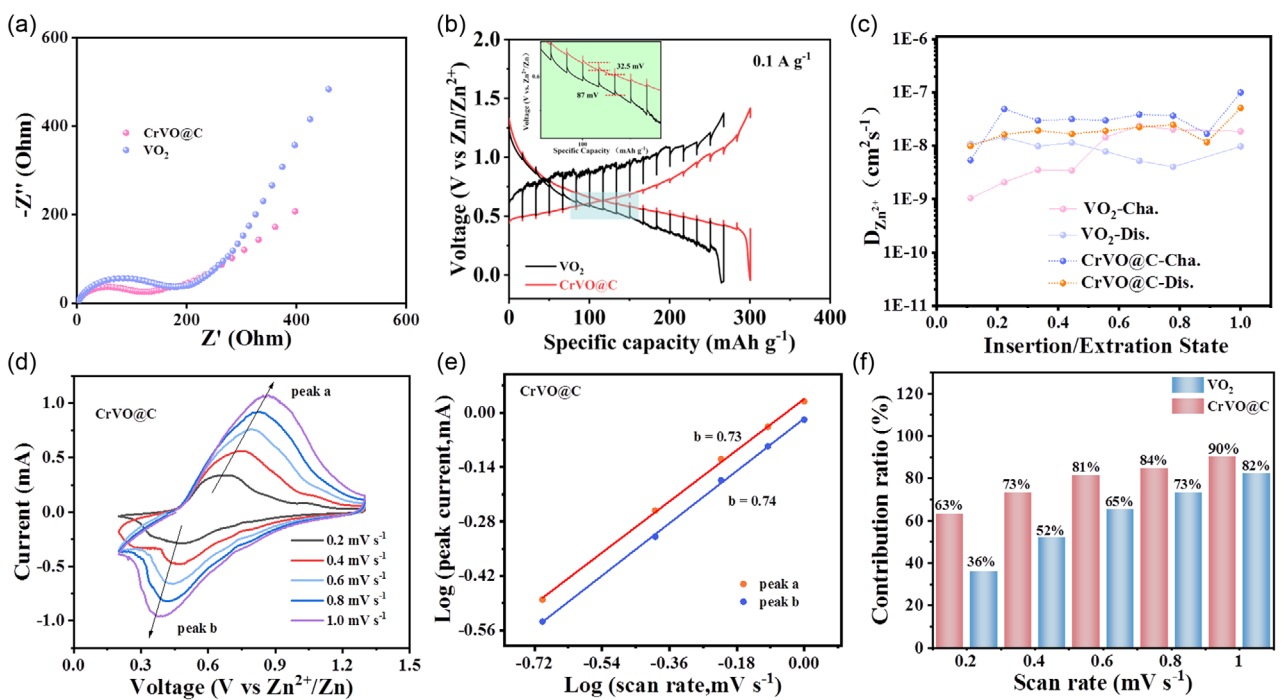


**Figure 4.** a) Nyquist diagram of VO<sub>2</sub> and CrVO@C samples. b) GITT curve of VO<sub>2</sub> and CrVO@C at the current density of 0.1 A g<sup>-1</sup>. c) Zn<sup>2+</sup> diffusion coefficients ( $D_{Zn^{2+}}$ ) of VO<sub>2</sub> and CrVO@C. d) CV curves of CrVO@C at various scan rates from 0.2 to 1.0 mV s<sup>-1</sup>. e) The linear fitting curves between log i and log v of the marked peaks at different scan rates. f) Capacitive contribution of CrVO@C and VO<sub>2</sub> cathode materials.

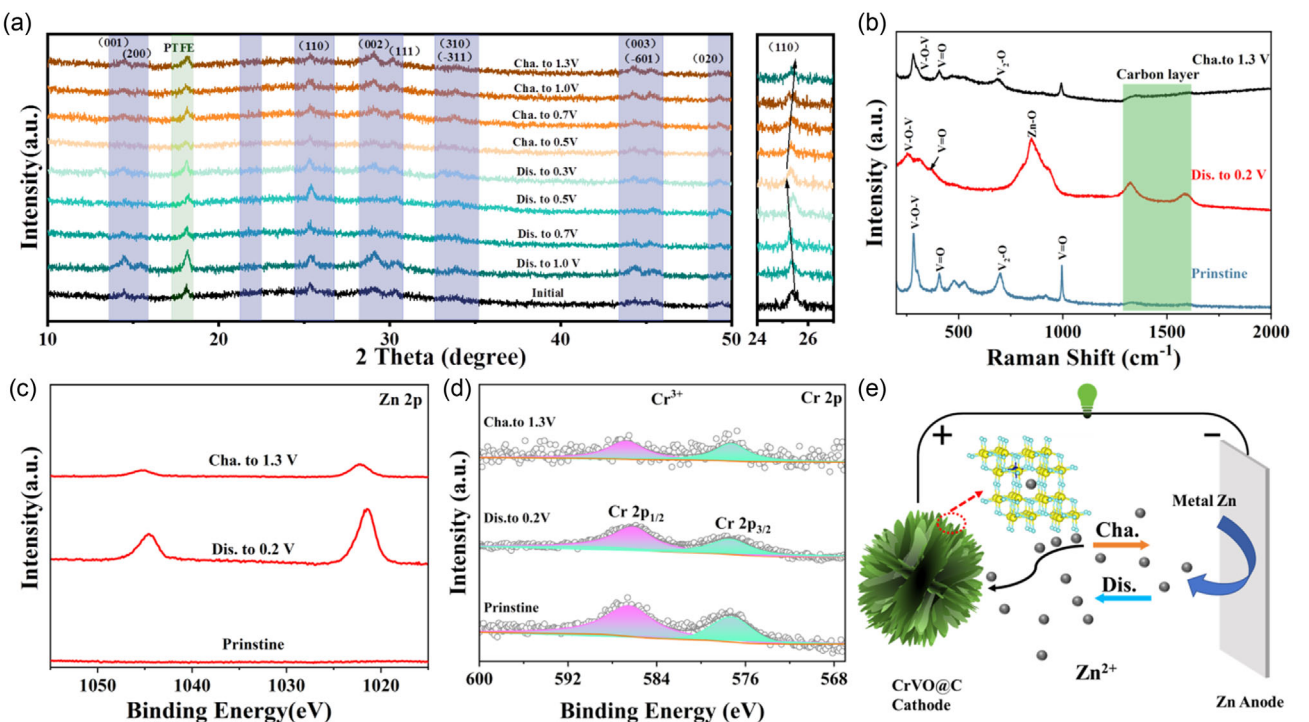


**Figure 5.** a) Ex situ XRD patterns of CrVO@C during the first discharging/charging process. b) Ex situ Raman spectrum of CrVO@C at initial, fully discharged, and charged states. c,d) Ex situ XPS spectra of Zn 2p and Cr 2p at initial, fully discharged, and charged states. e) The Schematic illustration of the operation mechanism in the CrVO@C/Zn battery.

Figure S3 and S4, Supporting Information, show that the CrVO@C and VO<sub>2</sub> had the capacitance contribution accounts for 90.1 and 72.39% at 1 mV s<sup>-1</sup>. This indicates that the electrochemical redox

reaction of the CrVO@C electrode is primarily dominated by the capacitance-controlled process, which is beneficial for enhancing electron/ion transfer kinetics.<sup>[19]</sup>

## 2.4. Zn<sup>2+</sup> Storage Mechanism

To gain deeper insights into the zinc-ion storage mechanism in the Zn//CrVO@C battery, ex situ XRD measurements were conducted on the Zn//CrVO@C battery at various cutoff voltages. As depicted in Figure 5a, during the discharge process, the intercalation of zinc ions leads to a gradual decline in the intensity of the diffraction peaks, accompanied by a discernible shift toward lower angles. Upon subsequent charging process, the intensity of these peaks reverts nearly to its original state, as evidenced by the behavior of the characteristic (110) crystal plane. This observation underscores the highly reversible nature of the zinc storage mechanism within the CrVO@C cathode material. Additionally, ex situ Raman spectroscopy was employed to monitor chemical bonding evolution during the cycling process (Figure 5b). Notably, when fully discharged to 0.2 V, a characteristic peak attributed to Zn<sub>x</sub>VO<sub>2</sub>·nH<sub>2</sub>O emerges at 840 cm<sup>-1</sup> and the reduced intensity of all V—O bonds; this peak subsequently shifts back to its original position upon reaching the fully charged state. This observation aligns with the ex situ XRD results and corroborates the reversible Zn<sup>2+</sup> insertion/extraction process.

Moreover, the ex situ XPS testing demonstrated that there are no zinc ion signals at the initial state within the CrVO@C cathode. However, when discharged to 0.2 V, the Zn 2p peaks were significantly enhanced at 1022.50 eV (Zn 2p<sub>3/2</sub>) and 1045.58 eV (Zn 2p<sub>1/2</sub>) due to the intercalation of Zn<sup>2+</sup> (Figure 5c). When charged to 1.3 V, the Zn signal was still detected due to the partially irreversible insertion of Zn<sup>2+</sup>, which weakened the signal intensity and may play a role in enhancing the structure stability.<sup>[20]</sup> Meanwhile, it was found that the intensity of the Cr signal (Figure 5d) slightly decreased during the discharge process, while its binding energy showed no obvious shift, indicating that Cr<sup>3+</sup> served merely as a dopant atom to modify the electronic structure. Therefore, as illustrated in Figure 5e, the zinc storage mechanism in the CrVO@C cathode is predominantly a typical zinc-ion intercalation/deintercalation mechanism.

## 3. Conclusions

In summary, we have successfully synthesized CrVO@C cathode materials with a unique sea urchin-like structure through a straightforward two-step hydrothermal method, incorporating chromium doping and carbon coating. The introduction of Cr<sup>3+</sup> ions significantly enhances the electrical conductivity of the material. Furthermore, the carbon coating contributes to the electrolyte–electrode interface stability. This dual protection strategy has helped VO<sub>2</sub> achieve outstanding electrochemical performance, including a capacity retention rate of 82.7% after 100 cycles at 0.1 A g<sup>-1</sup>, and 70% after 1000 cycles at 3 A g<sup>-1</sup>. Also, the enhanced Zn<sup>2+</sup> ion diffusion (about 1 e<sup>-8</sup> cm<sup>2</sup> s<sup>-1</sup>) and reduced overpotential were also achieved. This current strategy offers a considerable perspective on the synergistic regulation in cathode materials for aqueous zinc-ion batteries.

## Acknowledgements

This work was supported by the Natural Science Foundation of Hubei Province (2022CFA087).

## Conflict of Interest

The authors declare no conflict of interest.

## Data Availability Statement

The data that support the findings of this study are available in the supplementary material of this article.

**Keywords:** aqueous zinc-metal batteries • carbon coating • cathode materials • metal-ion doping • vanadium oxides

- [1] a) X. Jia, C. Liu, Z. G. Neale, J. Yang, G. Cao, *Chem. Rev.* **2020**, *120*, 7795; b) W. Zhang, W. Zhong, J. Wang, Q. An, L. Mai, *Adv. Energy Sustainability Res.* **2023**, *4*, 2300139; c) P. Ruan, S. Liang, B. Lu, H. J. Fan, J. Zhou, *Angew. Chem. Int. Ed.* **2022**, *61*, e202200598.
- [2] Z. Xing, G. Xu, J. Han, G. Chen, B. Lu, S. Liang, J. Zhou, *Trends Chem.* **2023**, *5*, 380.
- [3] a) W. Zhang, S. Zhu, T. Yang, L. Wu, J. Li, J. Liang, Y. Liu, L. Cui, C. Tang, X. Chen, H. Zhou, F. Qiao, M. Zhou, P. Luo, F. Chi, X. Liao, L. Zhang, Q. An, *Angew. Chem., Int. Ed.* **2025**, *64*, e202419732; b) S. Liu, J. He, D. Liu, M. Ye, Y. Zhang, Y. Qin, C. C. Li, *Energy Storage Mater.* **2022**, *49*, 93.
- [4] a) L. Xie, W. Xiao, X. Shi, J. Hong, J. Cai, K. Zhang, L. Shao, Z. Sun, *Chem. Commun.* **2022**, *58*, 13807; b) T.-T. Lv, X. Luo, G.-Q. Yuan, S.-Y. Yang, H. Pang, *Chem. Eng. J.* **2022**, *428*, 131211.
- [5] a) J. Yang, J. Cao, Y. Peng, W. Yang, S. Barg, Z. Liu, I. A. Kinloch, M. A. Bissett, R. A. Dryfe, *ChemSusChem* **2020**, *13*, 4103; b) S. Huang, S. He, H. Qin, X. Hou, *ACS Appl. Mater. Interfaces* **2021**, *13*, 44379.
- [6] a) J. Guo, B. He, W. Gong, S. Xu, P. Xue, C. Li, Y. Sun, C. Wang, L. Wei, Q. Zhang, Q. Li, *Adv. Mater.* **2024**, *36*, 2303906; b) Y. Liu, X. Wu, *Nano Energy* **2021**, *86*, 106124.
- [7] M. Guo, K. Ni, Y. Zhu, *Interdiscip. Mater.* **2024**, *3*, 189.
- [8] M. Liao, J. Wang, L. Ye, H. Sun, Y. Wen, C. Wang, X. Sun, B. Wang, H. Peng, *Angew. Chem., Int. Ed.* **2020**, *59*, 2273.
- [9] W. Zhang, J. Liu, W. Cai, M. Zhou, W. Zhong, G. Xiao, P. Luo, Y. Zhao, Q. An, *Chem. Eng. J.* **2023**, *464*, 142711.
- [10] M. Ma, R. Huang, M. Ling, Y.-S. Hu, H. Pan, *Interdiscip. Mater.* **2023**, *2*, 833.
- [11] Y. Zhang, L. Zhao, A. Chen, J. Sun, *Fundam. Res.* **2021**, *1*, 418.
- [12] T. Wang, W. Gao, Y. Zhao, S. Wang, W. Huang, *J. Mater. Sci. Technol.* **2024**, *173*, 107.
- [13] F. Liang, Z. Zou, S. Zhang, M. Chen, F. Yu, S. Jia, J. Nong, *J. Energy Storage* **2024**, *77*, 109787.
- [14] X. Chen, X. Zhai, Y. Wu, X. Wang, L. Zhang, C. Shang, H. Zhang, C. Zhao, J. Shang, D. Liu, *J. Energy Storage* **2025**, *114*, 115826.
- [15] W. Jiang, K. Zhu, W. Yang, *Chem. - A Eur. J.* **2023**, *29*, e202301769.
- [16] X. Dou, X. Xie, S. Liang, G. Fang, *Sci. Bull.* **2024**, *69*, 833.
- [17] a) P. Luo, W. Zhang, S. Wang, G. Liu, Y. Xiao, C. Zuo, W. Tang, X. Fu, S. Dong, *J. Alloys Compd.* **2021**, *884*, 161147; b) W. Sun, F. Wang, S. Hou, C. Yang, X. Fan, Z. Ma, T. Gao, F. Han, R. Hu, M. Zhu, C. Wang, *J. Am. Chem. Soc.* **2017**, *139*, 9775.
- [18] Y. Liu, Y. Liu, Y. Yamauchi, Z. A. Alothman, Y. V. Kaneti, X. Wu, *Batteries Supercaps* **2021**, *4*, 1867.
- [19] Y. Gao, J. Yin, X. Xu, Y. Cheng, *J. Mater. Chem. A* **2022**, *10*, 9773.
- [20] H. Jiang, Y. Zhang, L. Xu, Z. Gao, J. Zheng, Q. Wang, C. Meng, J. Wang, *Chem. Eng. J.* **2020**, *382*, 122844.

Manuscript received: May 1, 2025  
Revised manuscript received: June 13, 2025  
Version of record online: